



# $\pi$ - $\pi$ conjugation driving degradation of aromatic compounds with in-situ hydrogen peroxide generation over $\text{Zn}_2\text{In}_2\text{S}_5$ grown on nitrogen-doped carbon spheres

Cuiwei Du<sup>a</sup>, Weiwei Feng<sup>a</sup>, Shiyu Nie<sup>a</sup>, Xianfa Su<sup>a</sup>, Haijin Liu<sup>a</sup>, Jinglan Feng<sup>a</sup>, Jianhui Sun<sup>a,\*</sup>, Chun Hu<sup>a,b,\*\*</sup>, Shuying Dong<sup>a,\*</sup>

<sup>a</sup> School of Environment, Henan Normal University, Key Laboratory for Yellow River and Huai River Water Environmental and Pollution Control, Ministry of Education, Henan Key Laboratory for Environmental Pollution Control, Xinxiang, Henan 453007, PR China

<sup>b</sup> Institute of Environmental Research at Greater Bay, Key Laboratory for Water Quality and Conservation of the Pearl River Delta, Ministry of Education, Guangzhou University, Guangzhou 510006, PR China

## ARTICLE INFO

### Keywords:

$\text{Zn}_2\text{In}_2\text{S}_5/\text{NHCS}$   
Aromatic pollutant removal  
 $\text{H}_2\text{O}_2$  formed  
In situ sterilization  
 $\pi$ - $\pi$  interactions

## ABSTRACT

The water contaminant control with the simultaneous production of clean energy has been considered an ideal and sustainable strategy. Herein, a self-assembled  $\text{Zn}_2\text{In}_2\text{S}_5$  with N-doped hollow carbon spheres (NHCS) was first synthesized via in-situ hydrothermal method to achieve excellent performance for aromatic pollutant removal with high amounts of  $\text{H}_2\text{O}_2$  formed. Such a composite harvested phenol degradation efficiency of 97.6% with high  $\text{H}_2\text{O}_2$  yield of  $1.31 \text{ mmol L}^{-1}$ , and bisphenol A (BPA) degradation efficiency of 79.7% with high  $\text{H}_2\text{O}_2$  yield of  $2.31 \text{ mmol L}^{-1}$ . In addition, in-situ produced  $\text{H}_2\text{O}_2$  solution of composites achieved high-efficiency bacterial inactivation. Based on the characterization results, NHCS contained abundant aromatic frameworks of  $\pi$  conjugates with C—C and N-hybrid rings. Meanwhile, phenol or BPA with rich  $\pi$  bonds was tightly adsorbed to the photocatalyst surface through  $\pi$ - $\pi$  interactions, which resulted in decreased activation energy with surface-adsorbed phenol  $^*/\text{BPA}^*$ . The obtained electrons were quickly transferred to the dispersed dissolved oxygen accompanied by promoting the reduction of  $\text{O}_2$  into  $\text{H}_2\text{O}_2$ . This synergetic process was expected to develop novel photocatalysts towards water disinfection achieved the reuse of wastewater.

## 1. Introduction

With the unprecedented rapid growth of chemical and petrochemical industrialization in recent years, tremendous persistent organic pollutants (POPs) have been exposed into environment through varieties of industrial waste products [1–3]. Phenolic compounds as the basic industrial materials are a main series of POPs, which have a wide range of uses in pharmaceutical synthesis, phenolic resin production, and dyes synthesis, phenol and its derivatives are recognized the main ingredient in industrial effluent [4–6]. Conventional phenolic compounds remediation techniques such as adsorption, biodegradation and Fenton-oxidation are not found significant results and meet the strict regulations [7,8]. Therefore, it is urgently desirable to develop effective POPs remediation approaches from the ambient environment.

Semiconductor photocatalysis is powered by solar energy, emerging as a low-cost and renewable remediation strategy to photodegrade organic contaminants [9–11]. During the photocatalytic processes, photoexcited semiconductors can exceed the bandgap energy to generate large amounts of electron and hole (e-h) pairs for pollution degradation [12–14]. Particularly, semiconductors such as metal oxides, metal sulfides and their multi-composites exhibit superior photocatalytic performance towards POPs due to their unique physical and chemical properties [15,16].

Metal sulfides are composed of one or more metal elements incorporated with S element, which have suitable band position, outstanding optical ability and structural tunability [17–19]. Moreover, ternary metal sulfides have higher activity and more variable properties than binary metal sulfides [20].  $\text{Zn}_m\text{In}_2\text{S}_{3+m}$  materials ( $1 \leq m \leq 5$ ) as a

\* Corresponding authors.

\*\* Corresponding author at: School of Environment, Henan Normal University, Key Laboratory for Yellow River and Huai River Water Environmental and Pollution Control, Ministry of Education, Henan Key Laboratory for Environmental Pollution Control, Xinxiang, Henan 453007, PR China.

E-mail addresses: [sunjjhhj@163.com](mailto:sunjhhj@163.com) (J. Sun), [huchun@gzhu.edu.cn](mailto:huchun@gzhu.edu.cn) (C. Hu), [dongsy@htu.edu.cn](mailto:dongsy@htu.edu.cn) (S. Dong).

<https://doi.org/10.1016/j.apcatb.2022.121298>

Received 19 January 2022; Received in revised form 28 February 2022; Accepted 6 March 2022

Available online 8 March 2022

0926-3373/© 2022 Elsevier B.V. All rights reserved.

member of famous ternary metal sulfide have a similar crystal structure, the conduction band (CB) and valence band (VB) potential can be successfully controlled according to the ratio of Zn/In, in the process of synthesis [21].  $\text{Zn}_2\text{In}_2\text{S}_5$  has aroused comprehensive attention, Zhang et al. found that  $\text{Zn}_2\text{In}_2\text{S}_5$  nanosheets than did  $\text{ZnIn}_2\text{S}_4$  and  $\text{Zn}_3\text{In}_2\text{S}_6$  showed higher selectivity for ethylene glycol production under visible-light irradiation [22]. Wang et al. developed a hierarchical  $\text{Zn}_2\text{In}_2\text{S}_5/\text{Ti}_3\text{C}_2$  photocatalyst with photocatalytic tetracycline degradation and hydrogen generation in comparison to the pure  $\text{Zn}_2\text{In}_2\text{S}_5$  [23]. Nonetheless, the structural and cycle performance of pure  $\text{Zn}_2\text{In}_2\text{S}_5$  still unsatisfactory, it is essential to modulate it with a suitable material.

Carbon materials have developed into ideal photocatalysts for scientific researchers due to their unique electronic conductivity, marvelous chemical stability and high electron reservoir ability [24–26]. Copious researches have been committed to construct different morphologies of porous nanosheets, hollow one-dimensional nanotubes and three-dimensional (3D) nanosphere, etc [10,20,27]. It is worth noting that the N-doped hollow carbon spheres (NHCS) are one of the support materials, have recently attracted more attention on account of its low density, high surface area with abundant active sites and fast pathway for electron and ion transport [28]. The graphene-like alignment structure and triazine ring of NHCS can induce large  $\pi$  bond system, which can lead to high electron delocalization effect [10,29]. Up to date, the template-assisted method has been used to synthesize the microsphere structure, which needs costly and multistep operations with removal of the templates causing heavy contamination to the environment. Therefore, the one-step self-templating method is preferred to fabricate the carbon materials, and other nanoparticles are deposited uniformly on the surface of NHCS, which was conducive to improve electrons conduction efficiency, and doping of nitrogen atoms can retard available the charge recombination. For instance, Li et al. reported carbon nitride hollow spheres with high crystallization were successfully prepared to realize abundant photocatalytic hydrogen production and good BPA degradation [30]. Therefore, combining the above merits and controllability of the carbon material, the carefully morphological designed N-doped hollow carbon spheres as the substrate co-catalyst can be well matched with the  $\text{Zn}_2\text{In}_2\text{S}_5$ .

The degradation of aromatic molecules (as hole scavengers) with simultaneous  $\text{H}_2\text{O}_2$  generation is of special significance for the wastewater treatment.  $\text{H}_2\text{O}_2$  as one of common oxidant and sanitizer can directly change the permeability of cell membranes achieving the effect of bactericidal and bacteriostatic properties. Thus-produced  $\text{H}_2\text{O}_2$  satisfies an in-situ disinfection measure, holding practical promise for turning waste into treasure. Herein, to combine the advantages of  $\text{Zn}_2\text{In}_2\text{S}_5$  and carbon materials, we used facile one-pot polymerization route to prepare  $\text{Zn}_2\text{In}_2\text{S}_5$  nano-catalyst in situ on a 3D substrate support of N-doped hollow carbon spheres and applied to degrade phenolic compounds. The three-part novelties of this current work are as follows: (1) the well-constructed novel structure with multiple active sites advantages, and induced  $\pi$ - $\pi$  interaction between NHCS and phenolic compounds (oxygen atom of phenol is hybridized with  $\text{sp}^2$  with in the formation of large  $\pi$  bond because a pair of lone electrons and benzene carbon atoms form the delocalized bond). (2) its high abatement and mineralization rate of aromatic compounds (substitute of sacrificial agent) with the simultaneous production of  $\text{H}_2\text{O}_2$ . (3) a disinfection procedure using  $\text{H}_2\text{O}_2$  generated in situ turning wastewater into treasure of sanitizer. This work may provide a reliable way to solve problems with water pollution and simultaneously realize the disinfection, which will make the utilization of wastewater resources to be much more environmentally friendly.

## 2. Experimental section

### 2.1. Synthesis of NHCS/ $\text{Zn}_2\text{In}_2\text{S}_5$ composites

2 mmol  $\text{InCl}_3 \cdot x\text{H}_2\text{O}$  and 2 mmol  $\text{ZnSO}_4 \cdot 7\text{H}_2\text{O}$  were dissolved into

mixture A consisting of 20 mL glycerol and 30 mL deionized water until completely dissolved. Meanwhile, a certain percentage of SDS (sodium dodecyl sulfate), melamine and glucose were dispersed in 10 mL of deionized water B with ultrasonic oscillation 1 h. Then the solutions of A and B were mixed and added 10 mmol TAA (thioacetamide) with stirring constantly for another 1 h (500 rpm) and heated at 160 °C for 12 h in 100 mL Teflon-lined autoclave. In order to obtain various mass ratios of NHCS to  $\text{Zn}_2\text{In}_2\text{S}_5$ , the total mass of NHCS precursor added during the synthesis process caused the mass percentage of as-obtained hybrids to 0, 1, 5, 10 and 15 wt%, which were denoted ZIS, CZS-1, CZS-5, CZS-10 and CZS-15.

Preparation of NHCS: 0.06 g SDS, 2.88 g glucose and 0.08 g melamine were together dissolved in 30 mL of distilled water by ultrasonic dissolution 1 h, the mixture was transferred into autoclave and heated at 160 °C for 10 h. The resulting solid precipitates were washed with deionized water and absolute ethanol for several times and dried overnight in vacuum.

Preparation of  $\text{Zn}_2\text{In}_2\text{S}_5$ : 2 mmol  $\text{InCl}_3 \cdot x\text{H}_2\text{O}$  and 2 mmol  $\text{ZnSO}_4 \cdot 7\text{H}_2\text{O}$  were dissolved in 20 mL glycerol and 30 mL deionized water with stirring constantly for 30 min, then 10 mmol TAA was added in this mixture with stirring for another 1 h (500 rpm). The mixed solution was transferred to a 100 mL Teflon-lined autoclave and maintained at 180 °C for 12 h. After the product was rinsed for several times, it was dried in vacuum oven.

### 2.2. Characterization of photocatalysts

The characterization of the photocatalysts was shown in the [Supporting Information](#).

### 2.3. Photocatalytic test

The photocatalytic efficiency was measured through the degradation of phenol or bisphenol A (BPA) solution under LED light irradiation. In every experiment, 50 mg sample was put into the 50 mL 20 mg  $\text{L}^{-1}$  phenol or BPA solution. Before irradiation, the solution was agitated in the dark for 30 min with continuously  $\text{O}_2$  bubbling to get absorption-desorption equilibrium. Subsequently, about 3 mL suspension was taken out every 30 min and filtered by a 0.22  $\mu\text{m}$  drainage filtration membrane. The degradation efficiency and amount of  $\text{H}_2\text{O}_2$  produced over CZS-5 were also measured by different bandpass filters (450, 500, 650 nm). The concentration of phenol or BPA solution was detected by high-performance liquid chromatography (HPLC, LC2000). The mobile phase was methanol and water (70:30, v/v) with a flow rate of 1.0 mg  $\text{L}^{-1}$ , wavelength of 270 nm for phenol and 230 nm for BPA. Following, the potassium titanium (IV) colorimetric method was performed for the determination of the amount of  $\text{H}_2\text{O}_2$  production during the photocatalytic system. 1 mL of 0.05 M potassium titanium oxalate within 3 M  $\text{H}_2\text{SO}_4$  solution was added to the filtrate, after standing for 8 min, the wavelength at 405 nm was determined by UV-2900 spectrometer [31]. In addition, isopropanol (IPA, 10 mmol  $\text{L}^{-1}$ ), ammonium oxalate (AO, 10 mmol  $\text{L}^{-1}$ ) and benzoquinone (BQ, 0.1 mmol  $\text{L}^{-1}$ ) were used to trap hydroxyl radicals ( $\cdot\text{OH}$ ), holes ( $\text{h}^+$ ) and superoxide radical ( $\cdot\text{O}_2^-$ ) in the active species capture experiment, respectively [32].

### 2.4. Bacterial disinfection

The bacteria suspension of *Escherichia coli* DH5a was prepared and diluted according to the literature [8]. Firstly, the bacteria were cultivated on agar medium: peptone (5 g), agar (10 g), NaCl (5 g) and toniskin (2.5 g) were mixed in 500 mL ultra-pure water and heated until dissolution (pH = 7), the agar solution and all glassware were sterilized at 120 °C. Bacterial inactivation experiments were subsequently carried out using in-situ generated  $\text{H}_2\text{O}_2$  from above irradiated suspension of CZS-5. 15 mL of agar solution was poured into the culture medium, and different amounts of the filtrate solution (0 mL, 0.1 mL, 1.0 mL, 2.0 mL

containing in-situ generated  $\text{H}_2\text{O}_2$ ) were added to the bacterial suspension, subsequently grown aerobically in stationary phase at  $36^\circ\text{C}$  for 12 h. The inhibition ratio was performed according to the culturable bacterial density.

### 3. Results and discussion

#### 3.1. Pollutant degradation accompanied by in-situ generation of $\text{H}_2\text{O}_2$

Firstly, to study the  $\text{H}_2\text{O}_2$  formation of all samples, a set of control experiments were executed by selectively screening in Fig. S1: (i) a group with molecular oxygen; (ii) a group with molecular oxygen and  $\text{pH} = 2$  adjusted with HCl solution; (iii) a group with molecular oxygen and proton donor isopropanol and  $\text{pH} = 2$  adjusted with HCl solution (according to our previous report of the optimum condition for producing  $\text{H}_2\text{O}_2$  [33]). CZS-5 demonstrated optimal performance in these three control conditions, where the quantity of  $\text{H}_2\text{O}_2$  could produce  $0.404 \text{ mmol L}^{-1}$ ,  $0.391 \text{ mmol L}^{-1}$  and  $0.637 \text{ mmol L}^{-1}$  respectively after 180 min light irradiation. We found that  $\text{H}_2\text{O}_2$  production was less dependent on proton concentrations ( $\text{pH}$  value variation) and sacrificial agent, indicated that  $\text{H}_2\text{O}_2$  production from water was successfully achieved by CZS composites only with continuously  $\text{O}_2$  bubbling and visible light condition. Therefore, the subsequent photocatalytic experiments were carried out only under  $\text{O}_2$  bubbling in the dark to achieve absorption and desorption equilibrium.

The simultaneous implementation of pollution control and clean energy development has been performed by directly degrading wastewater with in-situ hydrogen peroxide production. Prior to light irradiation, all samples in phenol or BPA solution were subjected to dark reaction for 30 min (extended to 60 min) to search an equilibrium (Fig. S2). As shown in Fig. 1a-b, compared with the pure NHCS and ZIS, the degradation performance and  $\text{H}_2\text{O}_2$  production efficiency of CZS-5 in the phenol solution were highest, with degradation efficiency up to 97.6% and  $\text{H}_2\text{O}_2$  yield up to  $1.31 \text{ mmol L}^{-1}$ , respectively. And it had the highest  $\text{H}_2\text{O}_2$  production in wastewater, which was  $\sim 5.69$  folds higher than pure NHCS and 1.95 folds higher than pure ZIS. Fig. 1c-d showed the degradation efficiency and  $\text{H}_2\text{O}_2$  production rate of CZS-5 under different bandpass filters (450, 500, and 650 nm), and the corresponding degradation efficiency of phenol within 180 min reached 69.2%, 44.1% and 30.7%, with simultaneous  $\text{H}_2\text{O}_2$  yields were  $0.98 \text{ mmol L}^{-1}$ ,  $0.67 \text{ mmol L}^{-1}$  and  $0.39 \text{ mmol L}^{-1}$ . The wavelength distribution of different bandpass filters was shown in Fig. S4. Moreover, the detailed experiment conclusions of composites with different proportions in Fig S3a-c

and Table S1 showed when further increasing NHCS loading amount, the photocatalytic degradation efficiency and  $\text{H}_2\text{O}_2$  production were reduced on the contrary, probably excessive dopants produced new recombination centers to suppress the separation of photogenerated charge carriers [34].

Another widely used aromatic pollutant of BPA (Fig. 1d-f, Fig S3d-f and Table S2) showed the similar results. With the introduction of NHCS, the degradation efficiency and simultaneous production efficiency of  $\text{H}_2\text{O}_2$  were increased and reached the maximum of CZS-5 sample: the degradation rate could reach 79.7% in 180 min, and the constant of degradation rate was  $0.0065 \text{ min}^{-1}$ , nearly 9.56 times higher than that of pristine NHCS ( $6.79 \times 10^{-4} \text{ min}^{-1}$ ) and 1.41 times that of pristine ZIS ( $0.0046 \text{ min}^{-1}$ ); the  $\text{H}_2\text{O}_2$  yield synchronously increased to  $2.31 \text{ mmol L}^{-1}$ , which was  $\sim 4.71$  times of that produced by NHCS ( $0.49 \text{ mmol L}^{-1}$ ) and 1.38 times of that produced by ZIS ( $1.67 \text{ mmol L}^{-1}$ ). At the same time, the degradation efficiency of BPA within 180 min reached 53.9%, 48.6% and 27.3% under 450, 500, and 650 nm bandpass filters, with simultaneous  $\text{H}_2\text{O}_2$  yields were  $1.98 \text{ mmol L}^{-1}$ ,  $1.37 \text{ mmol L}^{-1}$  and  $1.19 \text{ mmol L}^{-1}$ . Apparently, CZS-5 exhibited certain photocatalytic activity under visible low-energy LED light with bandpass filters. The maximum  $\text{H}_2\text{O}_2$  concentration was reached when phenol or BPA was nearly completely degraded, this might be due to the fact that electron delocalization on the aromatic rings and  $\pi$ - $\pi$  interactions between aromatic rings and composites regulated the more photogenerated electrons to participate in photoreduction of dissolved oxygen, while strong electron-donating of -OH groups on aromatic rings were easily oxidized and degraded by holes. Moreover, the  $\text{H}_2\text{O}_2$  yield in BPA solution was higher than that in phenol solution due to stronger  $\pi$ - $\pi$  interactions based on biphenyl ring structure.

Interestingly, the in situ generated  $\text{H}_2\text{O}_2$  in phenol wastewater could reach photostationary after about 3 h, which made its use as an alternative for on-site inactivation of *E. coli* (Fig. 2I). Although the dosages of the water samples had slight variation, there was no additional *E. coli* colonies appeared on the dish after 12 h (except that the dosage was 0.1 mL). It was attributed to a surplus of  $\text{H}_2\text{O}_2$  in this inactivation process.

It is reported that the PL excitation and emission of phenol were around 270 nm and 296 nm [35]. Three-dimensional fluorescence excitation-emission-matrix spectra (3D EEMs) in Fig. 2a-d were employed to monitor the detailed phenol degradation behaviors by the CZS-5. The fluorescence signal of initial phenol solution was very strong. And intensity decreased gradually with prolonged light irradiation,

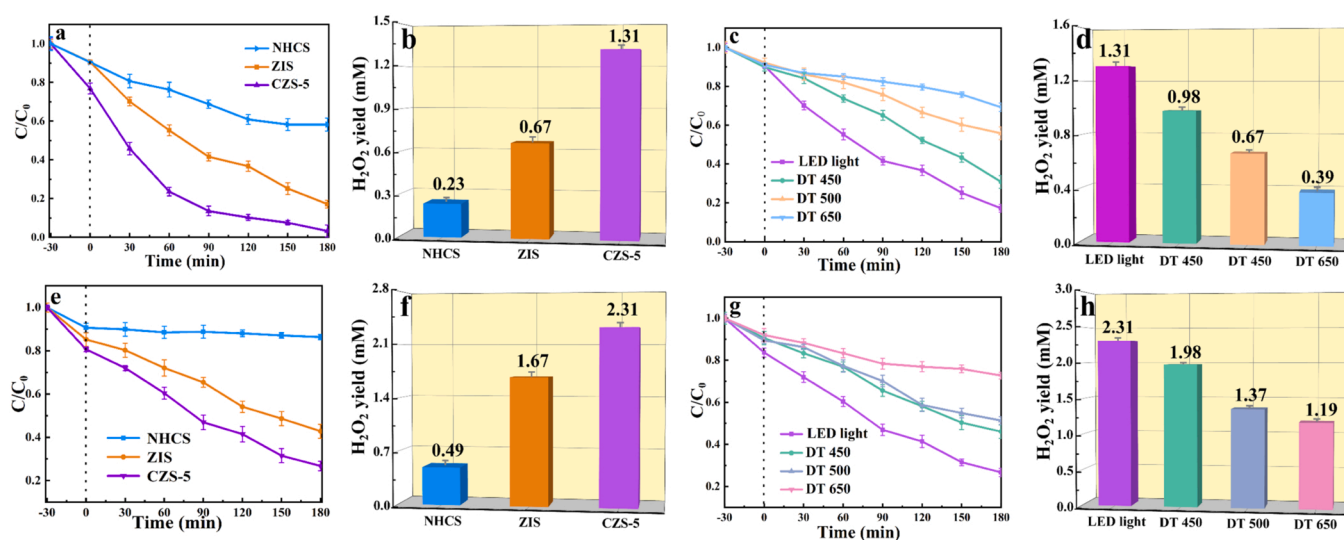
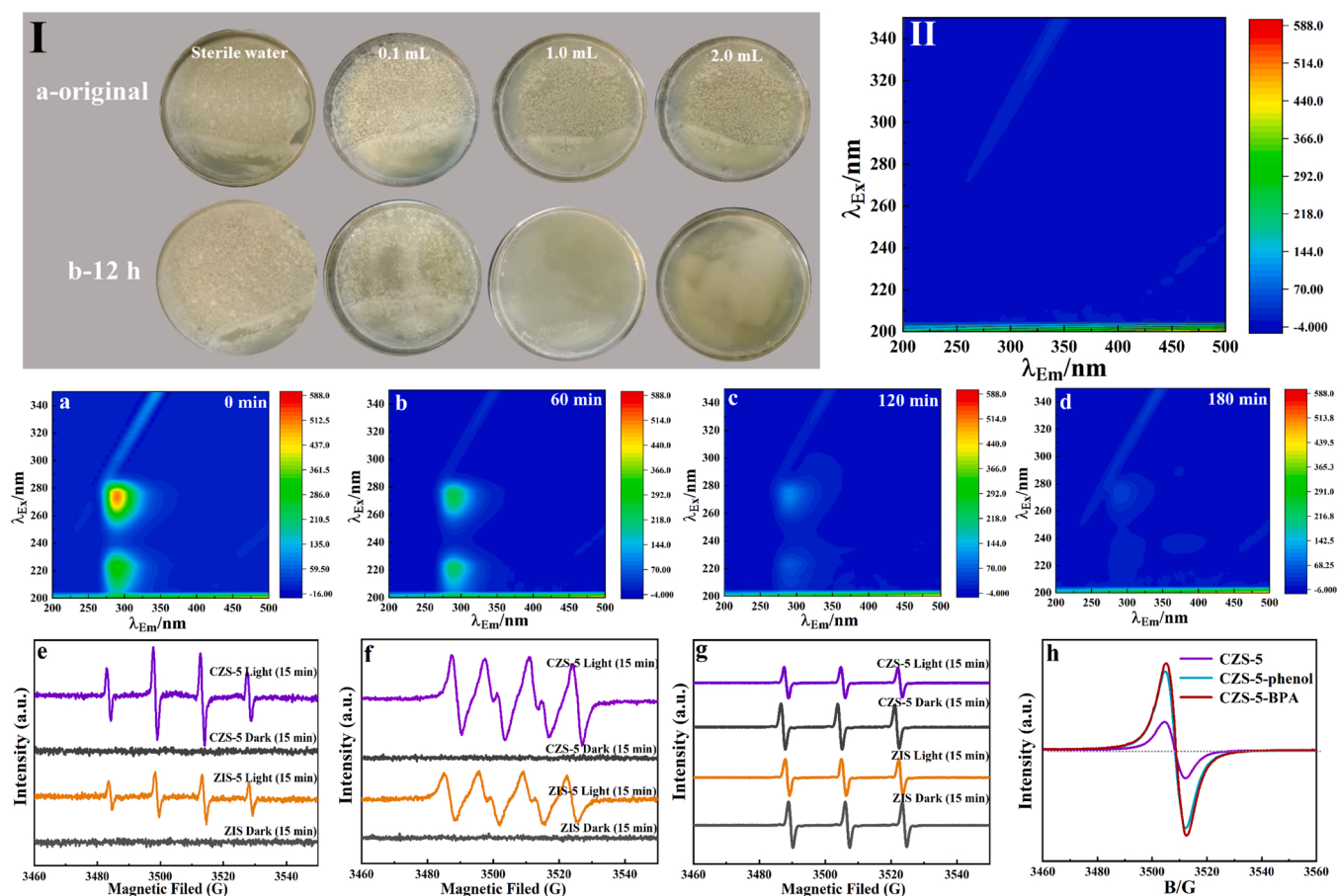


Fig. 1. (a–b) and (e–f) phenol or BPA degradation activities and the corresponding  $\text{H}_2\text{O}_2$  yields under 400 nm LED light irradiation; (c–d) and (g–h) CZS-5 phenol or BPA degradation activities and the corresponding  $\text{H}_2\text{O}_2$  yields under different single wavelength filters.



**Fig. 2.** (I) The disinfection of *E. coli* using the in-situ  $\text{H}_2\text{O}_2$  (different volume, mL) generated from the CZS-5 composite; (II) 3DEEM fluorescence spectra of pure water; (a-d) 3DEEM of the phenol ( $20 \text{ mg L}^{-1}$ ) degradation process using CZS-5 composite; EPR spectra of ZIS and CZS-5 (e)  $\bullet\text{OH}$ , (f)  $\bullet\text{O}_2^-$  and (g)  $\text{h}^+$  in dark reaction and photocatalysis process; (h) element ESR spectra of CZS-5 and absorbed phenol or BPA.

suggesting the gradual degradation of phenol, which was in consistent with the photocatalytic degradation results. The weak fluorescence signal could be observed after irradiation for 3 h that was similar to 3D EEM signal in pure water in Fig 2II, demonstrating intermediates could be further degraded during photocatalysis process.

The photocatalytic reusability problem can be greatly improved when the photocatalysis is performed without adjusting the pH. Therefore, the cycle stability of phenol degradation and simultaneous production of  $\text{H}_2\text{O}_2$  were investigated by CZS-5 sample (Fig. S5a). 87.13% phenol could still be degraded under four cycles, and the yield of  $\text{H}_2\text{O}_2$  produced could still reach  $1.12 \text{ mg L}^{-1}$ , which identified the high stability of the CZS materials. In addition, the total organic carbon (TOC) removal rates of NHCS, ZIS and CZS-5 were also determined, which were 16%, 44% and 87%, respectively (Fig. S5b).

In addition, to explore the main reactive species of CZS composite, the trapping experiments were implemented with ammonium oxalate (AO) as the hole ( $\text{h}^+$ ) scavenger, benzoquinone (BQ) as the superoxide radical ( $\bullet\text{O}_2^-$ ) scavenger and isopropanol (IPA) as the hydroxyl ( $\bullet\text{OH}$ ) scavenger. As shown in Fig. S5c, the degradation rate of CZS-5 could reach 97.6% within 180 min without the capture agent. When AO, BQ or IPA was added, the degradation performance was significantly suppressed, which meant that  $\bullet\text{OH}$ ,  $\bullet\text{O}_2^-$  and  $\text{h}^+$  were all major active species in the photodegradation process.

EPR technique was further confirm the presence of active radicals with DMPO as the probe agent. In Fig. 2e-g, no signal was detected under dark conditions for all the photocatalysts. Under 15 min visible light irradiation, the signals of the DMPO- $\bullet\text{OH}$  and DMPO- $\bullet\text{O}_2^-$  could be detected immediately, and the  $\bullet\text{OH}$  and  $\bullet\text{O}_2^-$  signals of CZS-5 composite

were much more prominent than that of the pristine ZIS sample due to more redox-active sites to promote charge transfer. Fig. 2 g showed that ZIS and CZS-5 all had obvious DMPO- $\text{h}^+$  peaks under dark conditions, and the intensity gradually became weak upon extending irradiation time, and the decay rate of CZS-5 was faster than that of ZIS. This indicated that  $\text{h}^+$  could directly participate in the photocatalytic degradation reaction. The EPR measurement was just consistent with the trapping experiments. In addition, EPR was used to investigate the trapped electrons in samples to further determine the influence of introducing absorbed phenol or BPA on the intrinsic electronic structure for CZS composites. The EPR showed that adsorbing phenol or BPA of CZS-5 sample exhibited excellent electron delocalization property with one single Lorentzian line of  $g = 2.003$  (Fig. 3h) [36]. An enhanced EPR signal of CZS-5-phenol or CZS-5-BPA indicated a much higher concentration of lone electron pair, which meant that the electrons of phenol or BPA were transferred to the NHCS ( $\pi$ )-rings via  $\pi$ - $\pi$  interactions [37]. Therefore, phenol or BPA introduction facilitated the production and separation of photogenerated charge carriers in CZS photocatalysts.

### 3.2. Mechanism discussion

The preparation route of CZS-X nano hollow bulb was shown in Fig. 3a. Firstly, the NHCS precursor solution and ZIS precursor solution were prepared, the mixtures were stirred to obtain the NHCS/ZIS dispersion, and kept heated for 12 h. The hollow bulb composite was obtained after washing and drying. The synthetic route of pure NHCS and  $\text{Zn}_2\text{In}_2\text{S}_5$  was also elucidated in Fig S6. The SEM and TEM images (Fig. 3b-d) characterized the morphology and elemental distribution of



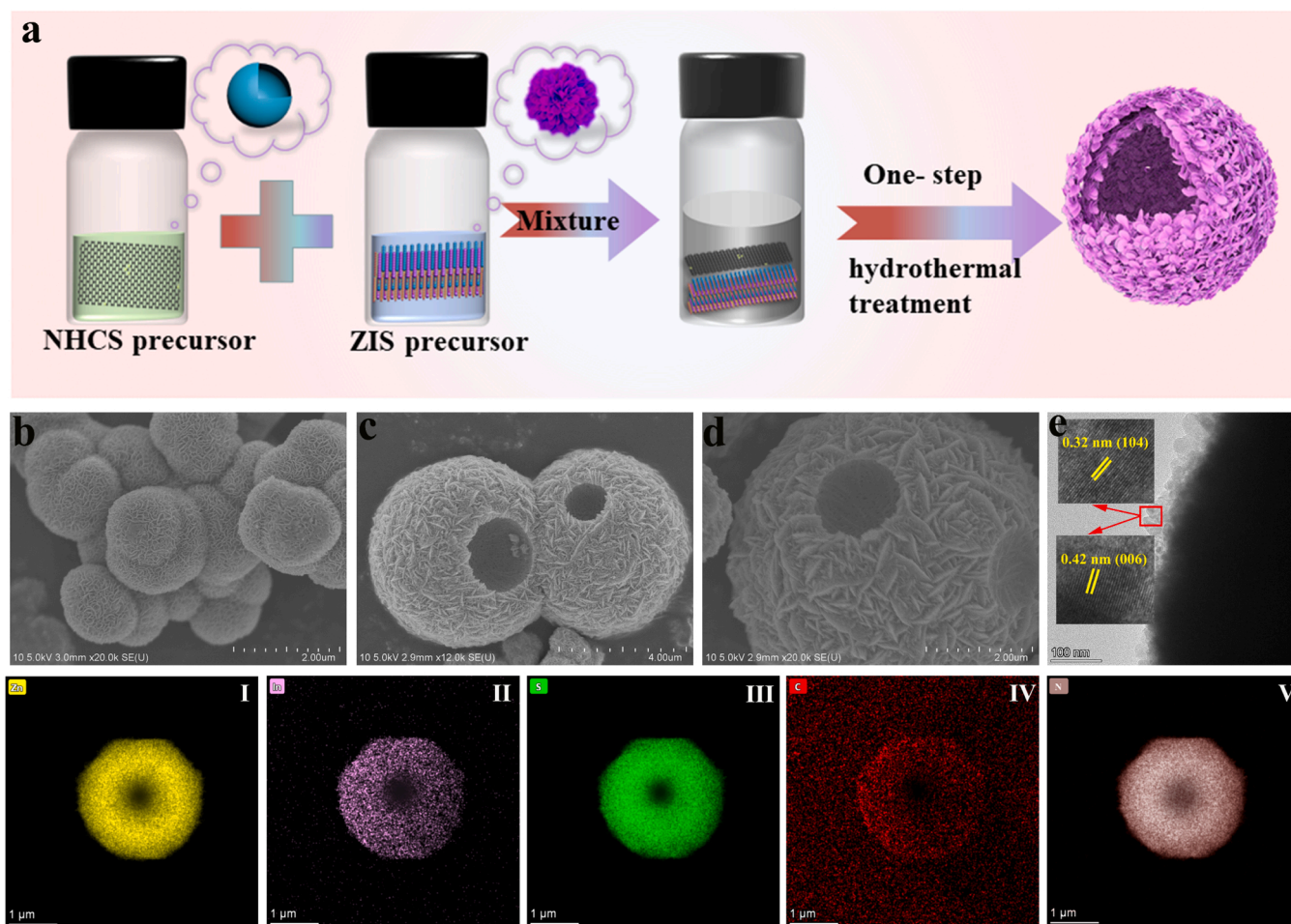


**Fig. 3.** Synthesis schematic illustration of CZS-X (a); SEM images of pure ZIS (b) and CZS-X (c, d); TEM images of the CZS-X (e); TEM-EDS elemental maps of CZS-X, uniformly distributed Zn, In, S, C and N (I–V).

the samples. Fig. S7 showed the hollow-shaped spheres of NHCS with diameters of 5–6  $\mu\text{m}$ .  $\text{Zn}_2\text{In}_2\text{S}_5$  in Fig. 3b displayed a 3D nanoflower structure with diameters of 1–2  $\mu\text{m}$ . It might be obvious to directly confirm from the SEM imaging that the ZIS nanosheets grew on the NHCS surface due to hollow spherical structure with arranging disordered nanosheet of composites in Fig. 3c–d. The composites could be further confirmed by high-resolution transmission electron microscopy in Fig. 3e, two kinds of stripe spacing of 0.32 nm and 0.42 nm corresponded respectively to the (104) facet and (006) facet of  $\text{Zn}_2\text{In}_2\text{S}_5$ . The element mapping in Fig. 3I–V and Fig. S9 showed the distribution of Zn,

In, S and C, N, O throughout the CZS-5. Moreover, as shown in Fig. S8, phenol was easily absorbed to the hollow part of CZS-X materials due to their more active sites and  $\pi$ - $\pi$  conjugation effect.

The XRD patterns (Fig. 4a) of ZIS and all CZS-X composites presented the similar profiles. XRD patterns for the NHCS powder revealed a broad hump at  $2\theta = 22^\circ$ , which suggested that NHCS possessed amorphous structure. The characteristic peaks located at  $21.3^\circ$ ,  $27.9^\circ$ ,  $28.9^\circ$ ,  $47.5^\circ$  and  $56.5^\circ$  were indexed respectively to the crystal planes of (102), (104), (112), and (202) of hexagonal  $\text{Zn}_2\text{In}_2\text{S}_5$ . The NHCS loading amount ranges from 1.0 to 15 wt%, and the characteristic peaks of NHCS

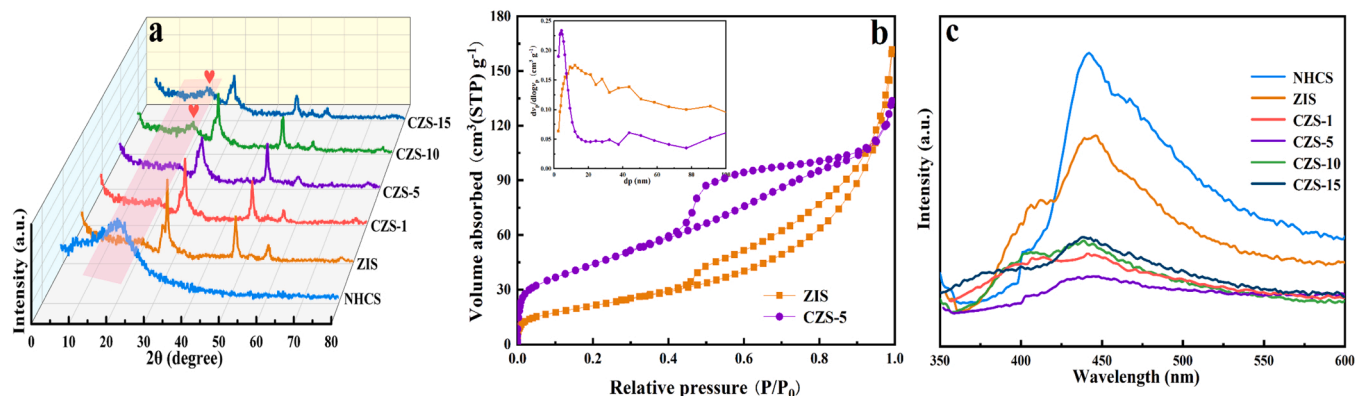


**Fig. 4.** (a) XRD pattern; (b) Nitrogen adsorption-desorption isotherms and corresponding pore size distributions; (c) PL spectra.

appeared when the loading amount reached 10%. In addition, the diffraction peaks of NHCS and  $\text{Zn}_2\text{In}_2\text{S}_5$  were significantly narrower in CZS-X composites, indicating the higher graphitization degree of carbon. The  $\text{N}_2$  adsorption-desorption isotherms were shown in Fig. 4b, both pure ZIS and CZS-5 exhibited mesoporous characteristic (belonging to type IV isotherm with the  $\text{H}_3$  hysteresis loop). The surface area and pore volume of CZS-5 were  $159.86 \text{ m}^2 \text{ g}^{-1}$  and  $0.239 \text{ cm}^3 \text{ g}^{-1}$ , respectively, which were higher than that of pure ZIS ( $78.39 \text{ m}^2 \text{ g}^{-1}$  and  $0.206 \text{ cm}^3 \text{ g}^{-1}$ , respectively), so that CZS composites might offer more reactive sites for enhancing the photocatalytic efficiency. The electron-hole recombination behavior was elucidated by PL spectra (Fig. 4c). The PL intensities of pure NHCS and ZIS were high, after both hybridized, the PL curve dramatically decreased in CZS composites, and the electron-hole separation efficiency: CZS-5 > CZS-1 > CZS-10 > CZS-15. This order followed the photocatalysis performance. Obviously, the CZS-5 curve was relatively flat, the reason of causing the low recombination rate was that CZS-5 possessed strong  $\pi$ - $\pi$  stacking interaction, which could induce low-energy excitonic transition and separation of electron-hole pairs.

To verify the chemical states and chemical interaction between NHCS and ZIS, X-ray photoelectron spectroscopy (XPS) was carried out in Fig. 5. For NHCS, the C 1s spectrum in Fig. 5a demonstrated the presence of C=C/C-C (284.8 eV), C-N/C-O (286.0 eV), and O-C=O/N-C=N (288.6 eV), and the peak of C=C/C-C revealed that  $\text{sp}^2$

hybridized C atoms could be transformed into the  $\pi$ -conjugated honeycomb lattice, which offered the possibility for the  $\pi$ - $\pi$  interaction between CZS and phenol [2]. The fitted N 1s spectrum (Fig. 5b) contained four components centered at 398.1, 399.9, 401.8, and 402.6 eV, corresponding to pyridinic, pyrrolic, graphitic, and nitrogen oxide, respectively [24]. Three peaks of O 1s spectrum (Fig. 5c) at 531.4, 532.7, and 533.7 eV were ascribed to the C=O, C-O/O-C-N, and C-OH groups, respectively. The characteristic peaks of C and N elements of NHCS and Zn, In and S elements of ZIS all existed in the CZS-5 composites in Fig. 5d-i, which indicated the well combination of NHCS and ZIS in composites. The binding energies of Zn 2p in Fig. 5d at 1022.1 and 1045.2 eV belonged to Zn 2p<sub>3/2</sub> and Zn 2p<sub>1/2</sub>, respectively, and the active binding energies of CZS-5 shifted to 1021.9 eV and 1045.0 eV, which suggested the extra coulombic interactions between the emitted electron and the zinc core [18,23]. The In 3d spectrum in Fig. 5e at 444.9 and 452.4 eV were corresponding to In 3d<sub>5/2</sub> and In 3d<sub>3/2</sub>, and the binding energy positions existed similar movement [38]. The S 2p peak in Fig. 5f at 161.8 and 162.9 eV were attributed to typically characteristic peaks in metal sulfide [39], and the apparent peak at 165.4 eV corresponded to C-S-C bond, this result could be attributed to the formation of bond of complex [40]. As for the C 1s spectrum of CZS-5, high-resolution XPS spectrum (Fig. 5g) exhibited that three C peaks were attributed to the C peaks of NHCS. According, a new peak at 287.3 eV belonged to C-S bond, which manifested that a certain

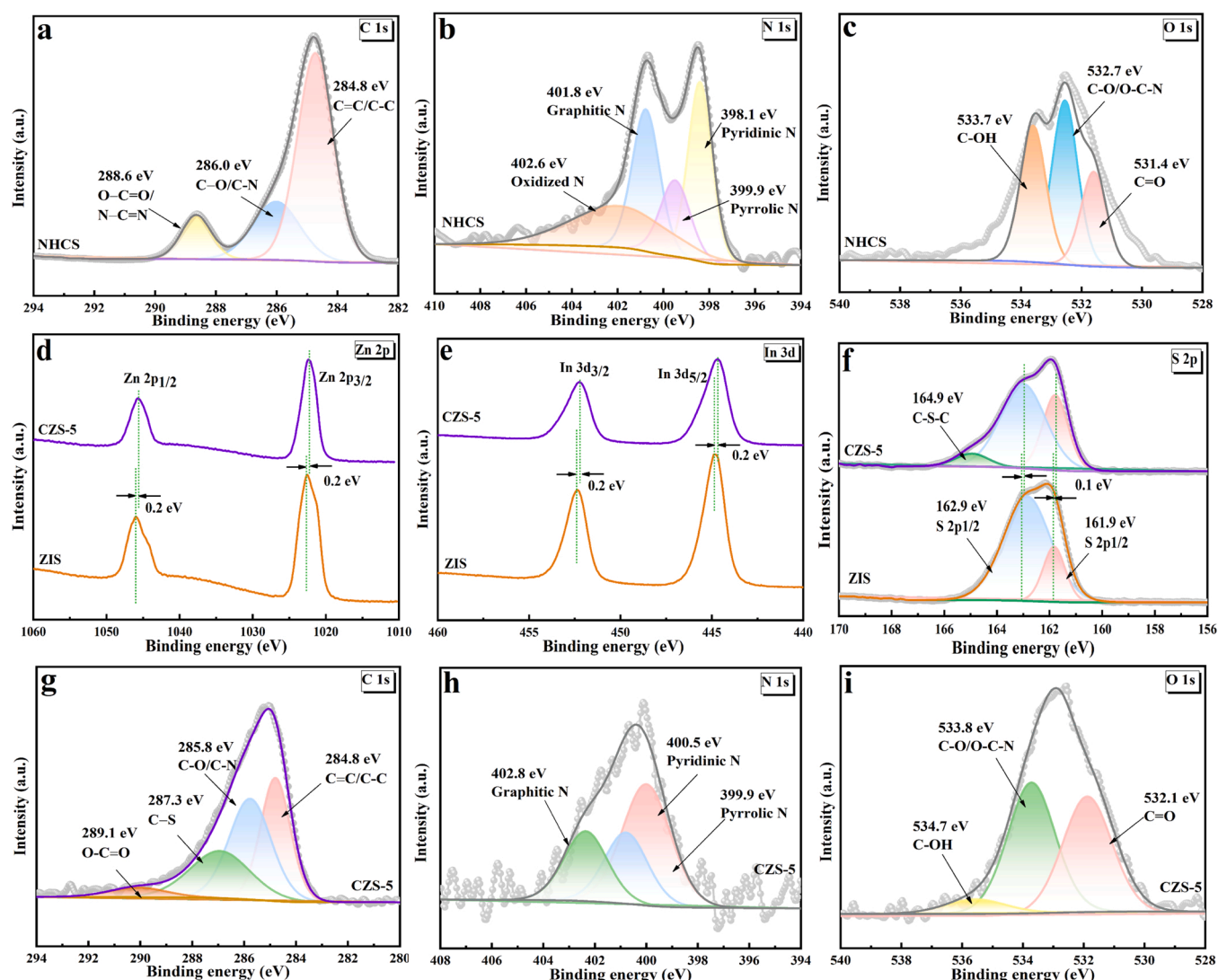


Fig. 5. (a-c) High-resolution C 1s, N 1s and O 1s spectra of NHCS. (d-i) Zn 2p, In 3d, S 2p and C 1s, N 1s and O 1s spectra of CZS-5.

proportion of NHCS was introduced into  $\text{Zn}_2\text{In}_2\text{S}_5$  [9,41,42]. The fitted peaks of N 1s spectrum in Fig. 2 h were slightly moved to 399.9 eV, 401.8 eV, and 402.8 eV, which were attributed to pyridinic, pyrrolic, graphitic [43,44]. The O 1s spectrum (Fig. 5i) could be deconvoluted into three peaks located at 532.1, 533.8 and 534.7 eV that were ascribed to the C—O, C—O/O—C—N and C—OH groups, respectively [45–47]. According to the above discussion, the CZS composites via C—S bond and conjugative  $\pi$ -bond could facilitate the electron transfer between NHCS and  $\text{Zn}_2\text{In}_2\text{S}_5$  [48].

To better comprehend the roles of phenol in pure ZIS and CZS composites catalytic process, the detail XPS spectra of phenol absorbed ZIS and CZS were displayed in Fig. S10 and Fig. 6. ZIS-phenol system in Fig. S10, the typical peaks of Zn 2p, In 3d, S 2s of  $\text{Zn}_2\text{In}_2\text{S}_5$  material and C 1s, O 1s of absorbed phenol were observed in the corresponding curves. The binding energies of Zn 2p in Fig. S10a were shifted to the direction of low binding energy in 0.1 eV, resulting in an increase of electron cloud density [49]. Moreover, it could be seen that Zn—O bond could be allocated to additional Zn—S bond from the peak shape of Zn 2p [50]. The peaks of In element and S element in Fig. S10b–c also moved slightly to lower binding energy value of 0.2 eV and 0.3 eV, respectively. The C 1s spectrum in Fig. S10d was classified into four components at 284.8 (C=C/C—C), 286.0 (C—O) and 288.6 eV (O—C=O), and carbon peak of Zn—O—C bond (283.6 eV) [40]. For O 1s spectrum due to the minor O-containing groups (Fig. S10e), the foremost peaks at 531.9 eV and 533.8 eV were in the form of lattice oxygen. In addition, the Zn—O (531.1 eV) bond and OH (533.7 eV) were found in ZIS-phenol material. All of these results illustrated the tight bond coupling between phenol and  $\text{Zn}_2\text{In}_2\text{S}_5$  substrate.

As for CZS-phenol system, the XPS spectra were similar to ZIS-phenol. In Fig. S11, the peaks of the C and O elements in CZS-phenol were increased, which might offer the possibility of  $\pi$ - $\pi$  interactions. Furthermore, the Zn/In/S molar ratios of CZS were similar at 1:0.8:2.4, further revealing the formation of  $\text{Zn}_2\text{In}_2\text{S}_5$  formula in composites. The detail XPS of Zn in fresh and absorbed CZS particles was displayed in Fig. 6a. The lower binding energy positions and more irregular peak pattern of Zn 2p than that of fresh CZS were described in CZS-5-phenol, and the peak of In, S elements and C, O, N elements in Fig. 6b–e also slightly shifted to lower binding energy. Compared to CZS-5 in Fig. 6d,

the C=C  $\text{sp}^2$  and C—O/C—N proportion of CZS-5-phenol were dropped, while the proportion of O—C=O/N—C=N increased, suggesting that more C=C and C—N bond converted into O—C=O/N—C=N for improving condensation degree of CZS-5-phenol, which provided more opportunities for  $\pi$ -electron delocalization [29]. Moreover, The N 1s spectrum of CZS-5-phenol was split into four peaks at 399.8 eV, 400.4 eV, 401.8 eV and 403.5 eV (Fig. 6e), with the former undoubtedly representing the pyridinic, pyrrolic and graphitic groups, and the latter representing a new peak that could be ascribed to the formation of  $\pi$ - $\pi$  excitations through sharing of a lone pair of electrons in the N atom and C atom, which implied the increased surface electron density in CZS-5-phenol composite [29]. It was also worth noting that the O 1s spectrum was composed of four chemical states including C—O, C—O/O—C—N, C—OH groups, and a new peak at 531.3 eV could be ascribed to the O atom coordination with  $\text{Zn}^{2+}$ . In other words, a few of zinc oxides might be generated on the surface of CZS-5-phenol. Thus, the appearance of new peaks ( $\pi$ - $\pi$  excitations and Zn—O bond) further confirmed that phenol could be well absorbed on CZS material via the surface functional groups.

In general, the adsorption of phenol by CZS sample could be analyzed as the following contributions: (a) the large specific surface areas and hollow structures of CZS could provide rich adsorption sites for harnessing phenol; (b) the surface metal groups of CZS had ability to combine phenolic hydroxyl groups in phenol through complexation; (c) the N heteroatoms and aromatic nucleus could activate the  $\pi$  electrons of CZS, mainly in the form of  $\pi$ - $\pi$  interactions between CZS and phenol. Therefore, the main adsorption properties between phenol and CZS was  $\pi$ - $\pi$  interactions and chemical bond. In addition, other functional groups (C—O, C—S, C—N and O—C=O, etc.) as adsorption points on the CZS were also crucial roles in the adsorption and degradation of phenol.

XPS spectra verified that CZS-5-phenol had rich oxygen-containing functional groups, which made it more hydrophilic. Therefore, the hydrophilicity of samples was performed in Fig. 7 by contact angle (CA) test. As we all know, the surface of photocatalyst is hydrophilic when the CA between water and photocatalyst is less than  $90.0^\circ$  [51]. The pure NHCS maintained super-hydrophobic performance (Fig. 7a), with CA greater than  $126.08^\circ$ . The CA of CZS-5 was  $48.79^\circ$  (Fig. 7e), which was lower than that of pure ZIS ( $70.99^\circ$ , Fig. 7c), suggesting that the surface

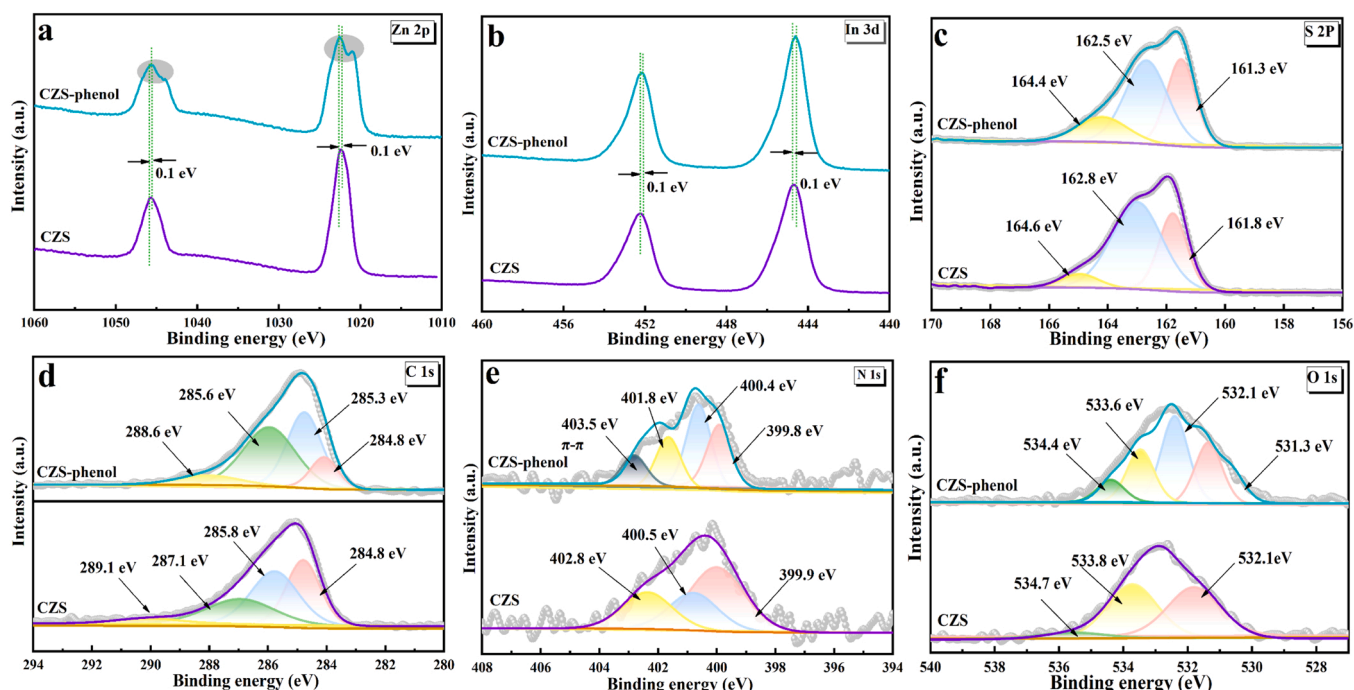


Fig. 6. XPS spectra (a) Zn 2p, (b) In 3d, (c) S 2p and (d) C 1s, (e) N 1s, (f) O 1s and C 1s, N 1s and O 1s spectra of CZS-5 and CZS-5 loaded with phenol.



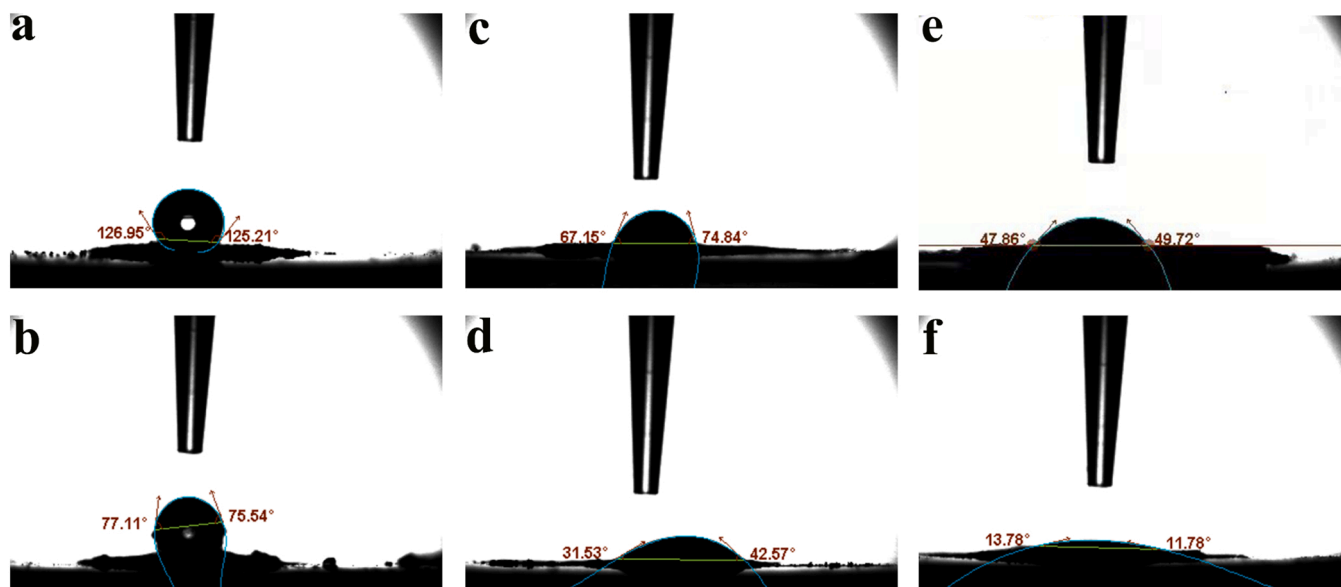


Fig. 7. Water-contact angles of NHCS (a, b), ZIS (c, d) and CZS-5 (e, f) before and after loading with phenol.

of CZS-5 was rougher and had larger specific surface areas than that of the ZIS. Notably, The CA of all samples decreased after introducing phenol with oxygen-containing functional groups, especially the CZS-5-phenol sample displayed a relatively small contact angle ( $12.78^\circ$ ), which was helpful to enhance the hydrophilicity, and facilitated the generation of  $\cdot\text{OH}$  to enhance the photocatalytic performance.

Theoretically, the graphitization of the NHCS was prone to form  $\pi$ - $\pi$  stacking structures, which can improve the separation of photo-generated electrons and holes for steadier photocatalysis [48]. The UV-vis DRS spectra were performed to investigate the optical properties, Fig. 8a showed that NHCS had excellent light absorption properties with wide wavelength range from 300 to 800 nm, as a result of black materials reduced the light reflectance. ZIS and CZS-5 possessed typical

semiconductor characteristics within wavelength range from 300 to 500 nm, the light absorption of CZS composites were higher than pure ZIS due to the introduction of black NHCS for incorporation of additional energy levels. Moreover, after absorbed phenol and BPA on the surface of samples, the red-shifted light absorption confirmed that phenol or BPA was successfully deposited on the sample surface, so that they could most effectively absorb light for the improvement of photocatalytic performance.

The band gaps calculated in Fig. S12a by the plots of  $(\text{Ah}\nu)^2$  versus  $h\nu$  were dramatically reduced from 2.67 to 2.32 eV of pure ZIS and CZS-5, suggesting that NHCS could introduce in the bulk structure of ZIS with a narrow intrinsic band gap due to the stronger  $\pi$ - $\pi$  stacking degree. Furthermore, the band gaps of CZS-5-phenol and CZS-5-BPA were

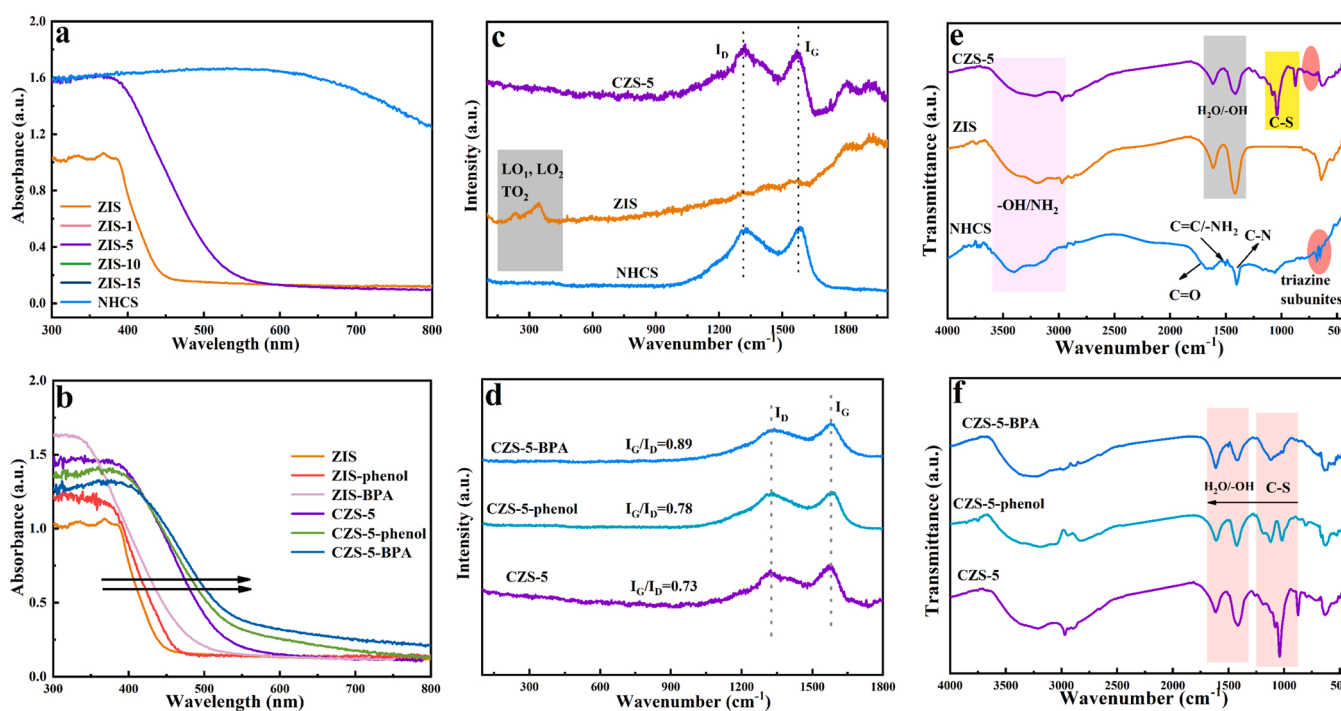


Fig. 8. (a, b) UV-vis diffuse reflection spectra of all synthesized sample before and after phenol absorption; (c, e) Raman spectra and FTIR spectra of NHCS, ZIS and CZS-5; (d, f) Raman spectra and FTIR spectra of CZS-5 and CZS-5 loaded with phenol.



calculated as 2.27 eV and 2.22 eV. The VB values were determined by XPS spectra (Fig. S12b) of ZIS and CZS-5 corresponded to 2.13 and 1.97 eV and CZS-5-phenol and CZS-5-BPA corresponded to 1.66 and 1.48 eV, respectively. Therefore, the  $E_{CB}$  of ZIS, CZS-5, CZS-5-phenol and CZS-5-BPA were calculated at  $-0.54$  eV,  $-0.35$  eV,  $-0.61$  eV and  $-0.74$  eV by the formula of  $E_{VB} = E_{CB} + E_g$  [52].

Raman technique and FTIR spectroscopy were applied to confirm different chemical functional groups and structural information between molecules in various synthesized samples. The Raman spectra (Fig. 8c) of ZIS sample showed characteristic Raman bands around  $200\text{--}300\text{ cm}^{-1}$ , which were related to the longitudinal and transverse optical modes ( $LO_1$ ,  $LO_2$  and  $TO_2$ ) of long wavelength lattice vibrations of  $Zn_2In_2S_5$  [53]. The CZS-5 and NHCS samples showed characteristic peaks at  $1350$  and  $1580\text{ cm}^{-1}$ , on the behalf of D peak (disordered carbon structure) and G peak (graphitized carbon structure), respectively. The G peak represented the degree of graphitization, which was prone to  $\pi$ - $\pi$  stacking inside the NHCS [54]. In other words,  $\pi$ - $\pi$  stacking degree could be evaluated by the value ratio of  $I_G/I_D$ . The ratio of  $I_G/I_D$  over the CZS was determined to be  $\sim 0.73$ , much higher than that observed over the NHCS (0.42), indicating ZIS could facilitate the ordered  $\pi$ - $\pi$  stacking degree of NHCS, which was conducive to long-range electron delocalization and migration [53]. After phenol or BPA absorption on the surface of CZS, the similar Raman spectra were depicted in Fig. 8d, the  $I_G/I_D$  value was 0.78 of CZS-5-phenol and  $I_G/I_D$  value was 0.89 of CZS-5-BPA, which were higher than that of CZS composites. The result indicated that the presence of more in-plane stretching vibration of  $sp^2$  hybridized carbon for the  $\pi$ - $\pi$  stacking over CZS-5-phenol and CZS-5-BPA [40].

The FTIR spectroscopy was carried out in Fig. 8e-f. For HCNS, the two typical characteristic peaks located at  $3000\text{--}3500\text{ cm}^{-1}$  and  $1000\text{--}1800\text{ cm}^{-1}$  could be ascribed to the vibration of O-H deformation vibrations or N-H bonds [55], and “quadrant or semicircle stretching” of aromatic C-N-C heterocycles, due to the hydrothermal process between melamine and glucose leading to the formation of the amide bond [41]. Other characteristic absorption band was related to the s-triazine and heptazine subunits at  $810\text{ cm}^{-1}$  [55]. The characteristic peaks at  $1610\text{ cm}^{-1}$  and  $1415\text{ cm}^{-1}$  both in pristine ZIS and CZS-5 could be related to the absorbed water molecules and hydroxyl groups hydroxyl groups [20]. The FT-IR spectrum of CZS had the characteristic peaks at  $800\text{--}900\text{ cm}^{-1}$  because of the existence of NHCS, further inducing stronger  $\pi$ - $\pi$  interaction in the CZS composites. In addition, the peaks of at  $1300\text{--}900\text{ cm}^{-1}$  could be ascribed to the C-S, indicating that the

composites introduced new binding mode between HCNS and ZIS [40], this was crucial for the electrons delocalization effect and further electrons transportation in the photocatalytic process. After phenol or BPA absorption on the surface of CZS, the similar FTIR results were depicted in Fig. 8f, all peaks in the active functional layer became weaker and displayed blue-shift, especially the O-H bond and C-S stretching frequency were shifted to a higher frequency region. These changes could be attributed to the presence of  $\pi$ - $\pi$  stacking effect between phenol and NHCS, resulting in changes in bond type and the bonding state and thereby decreasing the variation of dipole moment [29,56,57].

Based on the above discussion, the photodegradation mechanism of aromatic compound with in-situ  $H_2O_2$  generation in the CZS system could be proposed in Fig. 9 and illustrated by Eq. (1–7). Upon visible light irradiation, electrons were excited to the conduction band (CB) of CZS composite, holes thereby were thus left on the VB. Meanwhile, phenol or BPA was inclined to adsorb to the catalyst surface through  $\pi$ - $\pi$  interactions forming the surface-adsorbed phenol\* or BPA\*, and self  $\pi$ - $\pi$  stacking of CZS composites could further promote the electron delocalization effect, along the long-term transport pathway that could reduce the recombination rate of electrons and holes. The holes could easily spread out to catch phenol\* or BPA\* result in effective spatial charge separation. While the photogenerated electrons and delocalized electrons could transform the dissolved  $O_2$  to  $H_2O_2$ . The  $H_2O_2$  could also be further transferred into  $\bullet OH$ . In general, all reactive radicals participated in the degradation of phenol and reduction of electrons was the main route of  $H_2O_2$  production.

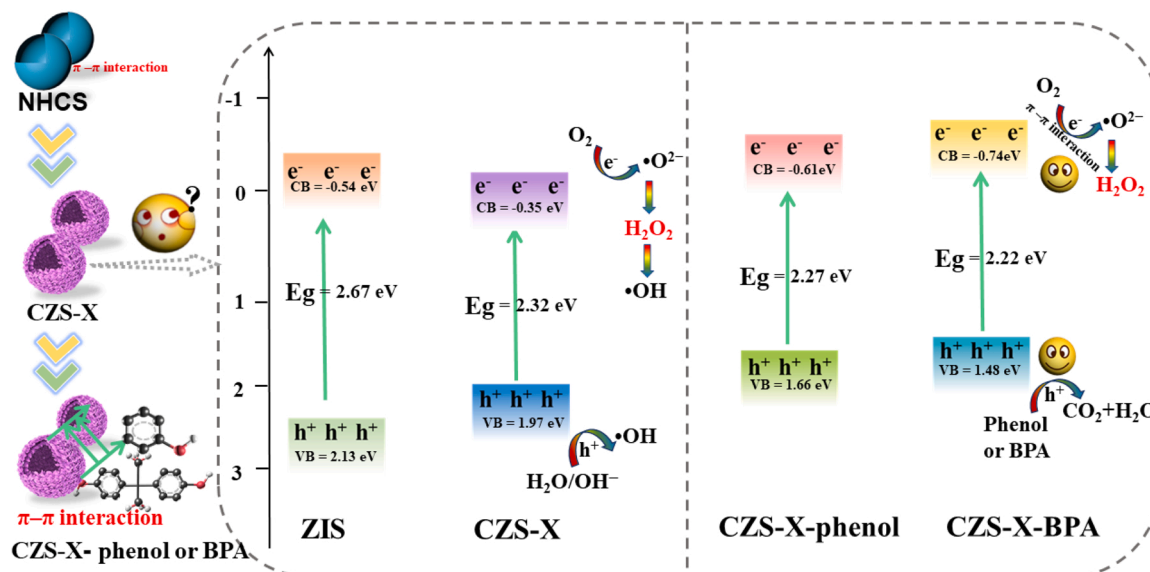
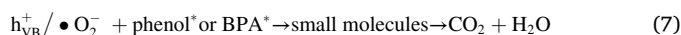
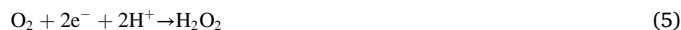
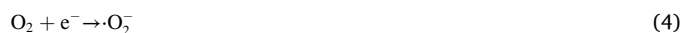
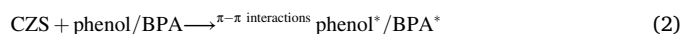


Fig. 9. Schematic diagram of the photodegradation with in-situ  $H_2O_2$  generation in the CZS-X/phenol system.

## 4. Conclusions

In summary, we prepared Zn<sub>2</sub>In<sub>2</sub>S<sub>5</sub> grown nitrogen-doped carbon spheres to achieve efficient water purification simultaneously with in situ generation of H<sub>2</sub>O<sub>2</sub>. The CZS-5 composites for photocatalytic degradation of phenol and BPA were significantly better than Zn<sub>2</sub>In<sub>2</sub>S<sub>5</sub> alone, and the H<sub>2</sub>O<sub>2</sub> yield could synchronously reach 1.31 mmol L<sup>-1</sup> and 2.31 mmol L<sup>-1</sup> in phenol and BPA solution respectively to achieve in situ sterilization. Combined with the XPS, Raman, FT-IR, and UV-vis spectra results of the reaction processes, pollutants were preferentially absorbed and degraded on the surface especially the holes of composites through  $\pi$ - $\pi$  interactions. The  $\pi$ - $\pi$  interaction between the CZS-5 composites and aromatic pollutants was helpful for the delocalization of the photogenerated electrons and improving anti-interference capability in different conditions. The delocalization electrons were rapidly transferred to the absorbed oxygen to generate free radicals assisted the efficient production of H<sub>2</sub>O<sub>2</sub>, which can be applied to the inactivation effect of bacteria to realize the reuse of wastewater. We expected this study might provide an interesting idea for the design of a modified photocatalyst to resolve water pollution with simultaneous disinfection as well as other important applications.

## CRediT authorship contribution statement

**Cuiwei Du:** Data curation, Writing – original draft. **Weiwei Feng:** Conceptualization, Writing – original draft. **Shiyu Nie:** Conceptualization, Writing – original draft. **Xianfa Su:** Theory analysis. **Haijin Liu:** Formal analysis. **Jinglan Feng:** Formal analysis. **Jianhui Sun:** Methodology, Funding acquisition. **Chun Hu:** Conceptualization, Writing – review & editing. **Shuying Dong:** Methodology, Funding acquisition.

## Declaration of Competing Interest

The authors declare that they have no known competing financial interests or personal relationships that could have appeared to influence the work reported in this paper.

## Acknowledgements

This work was supported by the NSFC (Grant nos. 22076039 and 22176051), the Postdoctoral Science Foundation, China (Grant nos. 2018M630825 and 2019T120624), excellent Science and Technology Innovation Team of Henan Normal University (2021TD03).

## Appendix A. Supporting information

Supplementary data associated with this article can be found in the online version at [doi:10.1016/j.apcatb.2022.121298](https://doi.org/10.1016/j.apcatb.2022.121298).

## References

- [1] M. Wagner, K.Y. Andrew Lin, W. Oh, G. Lisak, Metal-organic frameworks for pesticidal persistent organic pollutants detection and adsorption-a mini review, *J. Hazard. Mater.* 413 (2021), 125325, <https://doi.org/10.1016/j.jhazmat.2021.125325>.
- [2] S. Kumar, R. Kaushik, L. Purohit, Hetero-nanostructured Se-ZnO sustained with RGO nanosheets for enhanced photocatalytic degradation of p-chlorophenol, p-nitrophenol and methylene blue, *Sep. Purif. Technol.* 275 (2021), 119219, <https://doi.org/10.1016/j.seppur.2021.119219>.
- [3] Z. Winfield, F. Mansouri, C. Potter, R. Sabin, S. Trumble, S. Usenko, Eighty years of chemical exposure profiles of persistent organic pollutants reconstructed through baleen whale earplugs, *Sci. Total Environ.* 737 (2020), 139564, <https://doi.org/10.1016/j.scitotenv.2020.139564>.
- [4] T. Cheng, W. Zhang, W. Zhang, G. Yuan, H. Wang, T. Liu, An oleaginous filamentous microalgae *Tribonema minus* exhibits high removing potential of industrial phenol contaminants, *Bioresour. Technol.* 238 (2017) 749–754, <https://doi.org/10.1016/j.biortech.2017.05.040>.
- [5] A. Septian, A. Kumar, A. Sivasankar, J. Choi, I. Hwang, W. Shin, Colloidal activated carbon as a highly efficient bifunctional catalyst for phenol degradation, *J. Hazard. Mater.* 414 (2021), 125474, <https://doi.org/10.1016/j.jhazmat.2021.125474>.
- [6] J. Jin, J. Sun, K. Lv, X. Guo, Q. Hou, J. Liu, J. Wang, Y. Bai, X. Huang, Oxygen vacancy BiO<sub>2-x</sub>/Bi<sub>2</sub>WO<sub>6</sub> synchronous coupling with Bi metal for phenol removal via visible and near-infrared light irradiation, *J. Colloid Interface Sci.* 605 (2021) 342–353, <https://doi.org/10.1016/j.jcis.2021.06.085>.
- [7] J. Li, Y. Ren, F. Ji, B. Lai, Heterogeneous catalytic oxidation for the degradation of p-nitrophenol in aqueous solution by persulfate activated with CuFe<sub>2</sub>O<sub>4</sub> magnetic nano-particles, *Chem. Eng. J.* 324 (2017) 63–73, <https://doi.org/10.1016/j.cej.2017.04.104>.
- [8] J. Rodriguez, C. Gallampois, P. Haglund, S. Timonen, O. Rowe, Bacterial communities as indicators of environmental pollution by POPs in marine sediments, *Environ. Pollut.* 268 (2021), 115690, <https://doi.org/10.1016/j.envpol.2020.115690>.
- [9] T. Li, Y. Gao, L. Zhang, X. Xing, X. Huang, F. Li, Y. Jin, C. Hu, Enhanced Cr(VI) reduction by direct transfer of photo-generated electrons to Cr 3d orbitals in CrO<sub>4</sub><sup>2-</sup>-intercalated BiOBr with exposed (110) facets, *Appl. Catal. B-Environ.* 277 (2020), 119065, <https://doi.org/10.1016/j.apcatb.2020.119065>.
- [10] S. Dong, Y. Zhao, J. Yang, X. Liu, W. Li, L. Zhang, Y. Wu, J. Sun, J. Feng, Y. Zhu, Visible-light responsive PDI/rGO composite film for the photothermal catalytic degradation of antibiotic wastewater and interfacial water evaporation, *Appl. Catal. B-Environ.* 291 (2021), 120127, <https://doi.org/10.1016/j.apcatb.2021.120127>.
- [11] S. Lan, C. Yu, F. Sun, Y. Chen, D. Chen, W. Mai, M. Zhu, Tuning piezoelectric driven photocatalysis by La-doped magnetic BiFeO<sub>3</sub>-based multiferroics for water purification, *Nano Energy* 93 (2022), 106792, <https://doi.org/10.1016/j.nanoen.2021.106792>.
- [12] C. Du, S. Nie, C. Zhang, T. Wang, S. Wang, J. Zhang, C. Yu, Z. Lu, S. Dong, J. Feng, H. Liu, J. Sun, Dual-functional Z-scheme CdSe/Se/BiOBr photocatalyst: generation of hydrogen peroxide and efficient degradation of ciprofloxacin, *J. Colloid Interface Sci.* 606 (2022) 1715–1728, <https://doi.org/10.1016/j.jcis.2021.08.152>.
- [13] H. Liu, M. Chen, H. Zhang, B. Wang, J. Peng, G. Liu, One-step synthesis of hierarchical flower-like SnO<sub>2</sub>/BiOCCOOH microspheres with enhanced light response for the removal of pollutants, *Langmuir* 36 (2020) 9005–9013, <https://doi.org/10.1021/acs.langmuir.0c00025>.
- [14] W. Dai, L. Jiang, J. Wang, Y. Pu, Y. Zhu, Y. Wang, B. Xiao, Efficient and stable photocatalytic degradation of tetracycline wastewater by 3D polyaniline/perylene diimide organic heterojunction under visible light irradiation, *Chem. Eng. J.* 397 (2020), 125476, <https://doi.org/10.1016/j.cej.2020.125476>.
- [15] S. Dong, L. Cui, Y. Tian, L. Xia, Y. Wu, J. Yu, D.M. Bagley, J. Sun, M. Fan, A novel and high-performance double Z-scheme photocatalyst ZnO-SnO<sub>2</sub>-ZnSnO<sub>4</sub> for effective removal of the biological toxicity of antibiotics, *J. Hazard. Mater.* 399 (2020), 123017, <https://doi.org/10.1016/j.jhazmat.2020.123017>.
- [16] H. Liu, C. Du, M. Li, S. Zhang, H. Bai, L. Yang, S. Zhang, One-pot hydrothermal synthesis of SnO<sub>2</sub>/BiOBr heterojunction photocatalysts for the efficient degradation of organic pollutants under visible light, *ACS Appl. Mater. Interfaces* 10 (2018) 28686–28694, <https://doi.org/10.1021/acsami.8b09617>.
- [17] H. Wang, S. Naghadeh, C. Li, V. Cherrette, P. Fang, K. Xu, J. Zhang, Enhanced photoelectrochemical and photocatalytic properties of CdS nanowires decorated with NiS<sub>2</sub> nanoparticles under visible light irradiation, *J. Electrochem. Soc.* 166 (2019) H3146–H3153, <https://doi.org/10.1149/2.0211905jes>.
- [18] T. Gao, C. Lu, C. Hu, L. Lyu, H<sub>2</sub>O<sub>2</sub> inducing dissolved oxygen activation and electron donation of pollutants over Fe-ZnS quantum dots through surface electron-poor/rich microregion construction for water treatment, *J. Hazard. Mater.* 420 (2021), 126579, <https://doi.org/10.1016/j.jhazmat.2021.126579>.
- [19] X. Zou, D. Zhang, T. Luan, Q. Li, L. Li, P. Li, Y. Zhao, Incorporating photochromic triphenylamine into a zirconium-organic framework for highly effective photocatalytic aerobic oxidation of sulfides, *ACS Appl. Mater. Inter.* 13 (2021) 20137–20144, <https://doi.org/10.1021/acsami.1c03083>.
- [20] Z. Chen, F. Guo, H. Sun, Y. Shi, W. Shi, Well-designed three-dimensional hierarchical hollow tubular g-C<sub>3</sub>N<sub>4</sub>/ZnIn<sub>2</sub>S<sub>4</sub> nanosheets heterostructure for achieving efficient visible-light photocatalytic hydrogen evolution, *J. Colloid Interface Sci.* 607 (2021) 1391–1401, <https://doi.org/10.1016/j.jcis.2021.09.095>.
- [21] W. Fang, J. Liu, Y. Zhang, X. Li, N. Li, X. Zeng, W. Shangguan, Alkaline induced inorganic gradient distribution in Zn<sub>m</sub>In<sub>2</sub>S<sub>3+m</sub>/In(OH)<sub>3</sub> heterojunction for improved photocatalytic H<sub>2</sub> generation, *Appl. Surf. Sci.* 530 (2020), 147241, <https://doi.org/10.1016/j.apsusc.2020.147241>.
- [22] Y. Xie, Y. Li, Z. Huang, J. Zhang, X. Jia, X. Wang, J. Ye, Two types of cooperative nitrogen vacancies in polymeric carbon nitride for efficient solar-driven H<sub>2</sub>O<sub>2</sub> evolution, *Appl. Catal. B-Environ.* 265 (2020), 118581, <https://doi.org/10.1016/j.apcatb.2019.118581>.
- [23] H. Wang, Y. Sun, Y. Wu, W. Tu, S. Wu, X. Yuan, G. Zeng, Z. Xu, S. Li, J. Chew, Electrical promotion of spatially photoinduced charge separation via interfacial-built-in quasi-alloying effect in hierarchical Zn<sub>2</sub>In<sub>2</sub>S<sub>5</sub>/Ti<sub>3</sub>C<sub>2</sub>O<sub>4</sub> (OH)<sub>x</sub> hybrids toward efficient photocatalytic hydrogen evolution and environmental remediation, *Appl. Catal. B-Environ.* 245 (2019) 290–301, <https://doi.org/10.1016/j.apcatb.2018.12.051>.
- [24] Y. Wu, Z. Gao, Y. Feng, Q. Cui, C. Du, C. Yu, L. Liang, W. Zhao, J. Feng, J. Sun, R. Yang, J. Sun, Harnessing selective and durable electrosynthesis of H<sub>2</sub>O<sub>2</sub> over dual-defective yolk-shell carbon nanosphere toward on-site pollutant degradation, *Appl. Catal. B-Environ.* 298 (2021), 120572, <https://doi.org/10.1016/j.apcatb.2021.120572>.
- [25] Y. Yang, G. Zeng, D. Huang, C. Zhang, D. He, C. Zhou, W. Wang, W. Xiong, X. Li, B. Li, W. Dong, Y. Zhou, Molecular engineering of polymeric carbon nitride for highly efficient photocatalytic oxytetracycline degradation and H<sub>2</sub>O<sub>2</sub> production, *Appl. Catal. B-Environ.* 272 (2020), 118970, <https://doi.org/10.1016/j.apcatb.2020.118970>.

- [26] Z. Wang, Q. Wu, J. Zhang, H. Zhang, J. Feng, S. Dong, J. Sun, In situ polymerization of magnetic graphene oxide-diaminopyridine composite for the effective adsorption of Pb(II) and application in battery industry wastewater treatment, *Environ. Sci. Pollut. Res.* 26 (2019) 33427–33439, <https://doi.org/10.1007/s11356-019-06511-1>.
- [27] J. Chang, S. Zang, J. Li, D. Wu, Z. Lian, F. Xu, K. Jiang, Z. Gao, Nitrogen-doped porous carbon encapsulated nickel iron alloy nanoparticles, one-step conversion synthesis for application as bifunctional catalyst for water electrolysis, *Electrochim. Acta* 389 (2021), 138785, <https://doi.org/10.1016/j.electacta.2021.138785>.
- [28] H. Zhang, L. Zhao, L. Wang, J. Hao, X. Meng, Fabrication of oxygen-vacancy-rich black-BiOBr/BiOBr heterojunction with enhanced photocatalytic activity, *J. Mater. Sci.* 55 (2020) 10785–10795, <https://doi.org/10.1007/s10853-020-04700-9>.
- [29] R. Tang, D. Gong, Y. Deng, S. Xiong, J. Zheng, L. Li, Z. Zhou, L. Su, J. Zhao, pi-pi stacking derived from graphene-like biochar/g-C<sub>3</sub>N<sub>4</sub> with tunable band structure for photocatalytic antibiotics degradation via peroxymonosulfate activation, *J. Hazard. Mater.* 423 (2022), 126944, <https://doi.org/10.1016/j.jhazmat.2021.126944>.
- [30] Y. Li, D. Zhang, J. Fan, Q. Xiang, Highly crystalline carbon nitride hollow spheres with enhanced photocatalytic performance, *Chin. J. Catal.* 42 (2021) 627–636, [https://doi.org/10.1016/S1872-2067\(20\)63684-1](https://doi.org/10.1016/S1872-2067(20)63684-1).
- [31] L. Liang, M. Zhou, X. Lu, P. Su, J. Sun, High-efficiency electrogeneration of hydrogen peroxide from oxygen reduction by carbon xerogels derived from glucose, *Electrochim. Acta* 320 (2019), 134569, <https://doi.org/10.1016/j.electacta.2019.134569>.
- [32] J. Xiong, X. Lia, J. Huang, X. Gao, Z. Chen, J. Liu, H. Li, B. Kang, W. Yao, Y. Zhu, CN/rGO@BPQDs high-low junctions with stretching spatial charge separation ability for photocatalytic degradation and H<sub>2</sub>O<sub>2</sub> production, *Appl. Catal. B-Environ.* 266 (2020), 118602, <https://doi.org/10.1016/j.apcatb.2020.118602>.
- [33] C. Du, W. Feng, S. Nie, J. Zhang, Y. Liang, X. Han, Y. Wu, J. Feng, S. Dong, H. Liu, J. Sun, Harnessing efficient in-situ H<sub>2</sub>O<sub>2</sub> production via a KPf<sub>6</sub>/BiOBr photocatalyst for the degradation of polyethylene, *Sep. Purif. Technol.* 279 (2021), 119734, <https://doi.org/10.1016/j.seppur.2021.119734>.
- [34] H. Dong, Y. Zuo, N. Song, S. Hong, M. Xiao, D. Zhu, J. Sun, G. Chen, C. Li, Bimetallic synergetic regulating effect on electronic structure in cobalt/vanadium co-doped carbon nitride for boosting photocatalytic performance, *Appl. Catal. B-Environ.* 287 (2021), 119954, <https://doi.org/10.1016/j.apcatb.2021.119954>.
- [35] H. Ou, C. Wei, C. Mo, H. Wu, Y. Ren, C. Feng, Novel insights into anoxic/aerobic<sup>1</sup>/aerobic<sup>2</sup> biological fluidized-bed system for coke wastewater treatment by fluorescence excitation-emission matrix spectra coupled with parallel factor analysis, *Chemosphere* 113 (2014) 158–164, <https://doi.org/10.1016/j.chemosphere.2014.04.102>.
- [36] W. Ho, Z. Zhang, W. Lin, S. Huang, X. Zhang, X. Wang, Y. Huang, Copolymerization with 2,4,6-triaminopyrimidine for the rolling-up the layer structure, tunable electronic properties, and photocatalysis of g-C<sub>3</sub>N<sub>4</sub>, *ACS Appl. Mater. Inter.* 7 (2015) 5497–5505, <https://doi.org/10.1021/am509213x>.
- [37] Y. Li, R. Jin, Y. Xing, J. Li, S. Song, X. Liu, M. Li, R. Jin, Macroscopic foam-like holey ultrathin g-C<sub>3</sub>N<sub>4</sub> nanosheets for drastic improvement of visible-light photocatalytic activity, *Adv. Energy Mater.* 6 (2016) 1601273, <https://doi.org/10.1002/aenm.201601273>.
- [38] H. Liu, C. Niu, H. Guo, C. Liang, D. Huang, L. Zhang, Y. Yang, L. Li, In suit constructing 2D/1D MgIn<sub>2</sub>S<sub>4</sub>/CdS heterojunction system with enhanced photocatalytic activity towards treatment of wastewater and H<sub>2</sub> production, *J. Colloid Interface Sci.* 576 (2020) 264–279, <https://doi.org/10.1016/j.jcis.2020.05.025>.
- [39] Q. Liang, S. Cui, C. Liu, S. Xu, C. Yao, Z. Li, Construction of CdS@UO-66-NH<sub>2</sub> core-shell nanorods for enhanced photocatalytic activity with excellent photostability, *J. Colloid Interface Sci.* 524 (2018) 379–387, <https://doi.org/10.1016/j.jcis.2018.03.114>.
- [40] Y. Zhang, G. Zhao, L. Gan, H. Lian, M. Pan, S-doped carbon nanosheets supported ZnO with enhanced visible-light photocatalytic performance for pollutants degradation, *J. Clean. Prod.* 319 (2021), 128803, <https://doi.org/10.1016/j.jclepro.2021.128803>.
- [41] X. Ma, C. Chang, Y. Zhang, P. Niu, X. Liu, S. Wang, L. Li, Synthesis of Co-based prussian blue analogues/dual-doped hollow carbon microsphere hybrids as high-performance bifunctional electrocatalysts for oxygen evolution and overall water splitting, *ACS Sust. Chem. Eng.* 8 (2020) 8318–8326, <https://doi.org/10.1021/acssuschemeng.0c01974>.
- [42] M. Feng, J. Yan, B. He, X. Chen, J. Sun, Controllable conversion of shrimp shells into chitin or derived carbon material using acidic deep eutectic solvent, *Int. J. Biol. Macromol.* 193 (2021) 347–357, <https://doi.org/10.1016/j.ijbiomac.2021.10.122>.
- [43] C. Cheng, D. Chen, N. Li, Q. Xu, H. Li, J. He, J. Lu, ZnIn<sub>2</sub>S<sub>4</sub> grown on nitrogen-doped hollow carbon spheres: an advanced catalyst for Cr(VI) reduction, *J. Hazard. Mater.* 391 (2020), 122205, <https://doi.org/10.1016/j.jhazmat.2020.122205>.
- [44] Y. Xia, B. Cheng, J. Fan, J. Yu, G. Liu, Near-infrared absorbing 2D/3D ZnIn<sub>2</sub>S<sub>4</sub>/N-doped graphene photocatalyst for highly efficient CO<sub>2</sub> capture and photocatalytic reduction, *Sci. China Mater.* 63 (2020) 552–565, <https://doi.org/10.1007/s40843-019-1234-x>.
- [45] J. Zhao, M. Ji, J. Di, Y. Zhang, M. He, H. Li, J. Xia, Novel Z-scheme heterogeneous photo-Fenton-like g-C<sub>3</sub>N<sub>4</sub>/FeOCl for the pollutants degradation under visible light irradiation, *J. Photoch. Photobiol. A* 391 (2020), 112343, <https://doi.org/10.1016/j.jphotochem.2019.112343>.
- [46] G. Zuo, B. Li, Z. Guo, L. Wang, F. Yang, W. Hou, S. Zhang, P. Zong, S. Liu, X. Meng, Y. Du, T. Wang, V. Roy, Efficient photocatalytic hydrogen peroxide production over TiO<sub>2</sub> passivated by SnO<sub>2</sub>, *Catalysts* 9 (2019) 623, <https://doi.org/10.3390/catal9070623>.
- [47] S. Ingavale, P. Marbaniang, B. Kakade, A. Swami, Starbon with Zn-N and Zn-O active sites: an efficient electrocatalyst for oxygen reduction reaction in energy conversion devices, *Catal. Today* 370 (2021) 55–65, <https://doi.org/10.1016/j.cattod.2020.11.016>.
- [48] Y. Wei, M. Ma, W. Li, J. Yang, H. Miao, Z. Zhang, Y. Zhu, Enhanced photocatalytic activity of PTCDI-C<sub>60</sub> via  $\pi$ - $\pi$  interaction, *Appl. Catal. B-Environ.* 238 (2018) 302–308, <https://doi.org/10.1016/j.apcatb.2018.07.043>.
- [49] L. Liu, S. Liu, L. Zhao, G. Su, X. Liu, H. Peng, J. Xue, A. Tang, Fabrication of novel magnetic core-shell chelating adsorbent for rapid and highly efficient adsorption of heavy metal ions from aqueous solution, *J. Mol. Liq.* 313 (2020), 113593, <https://doi.org/10.1016/j.molliq.2020.113593>.
- [50] E. Amdeha, R. Mohamed, A. Dhmees, Sonochemical assisted preparation of ZnS-ZnO/MCM-41 based on blast furnace slag and electric arc furnace dust for Cr(VI) photoreduction, *Ceram. Int.* 47 (2021) 23014–23027, <https://doi.org/10.1016/j.ceramint.2021.05.015>.
- [51] Z. Xiong, Z. He, S. Mahmud, Y. Yang, L. Zhou, C. Hu, S. Zhao, Simple amphoteric charge strategy to reinforce superhydrophilic polyvinylidene fluoride membrane for highly efficient separation of various surfactant-stabilized oil-in-water emulsions, *ACS Appl. Mater. Interfaces* 12 (2020) 47018–47028, <https://doi.org/10.1021/acsaami.0c13508>.
- [52] C. Du, S. Nie, W. Feng, J. Zhang, M. Qi, Y. Liang, Y. Wu, J. Feng, S. Dong, H. Liu, J. Sun, Hydroxyl regulating effect on surface structure of BiOBr photocatalyst toward high-efficiency degradation performance, *Chemosphere* 287 (2021), 132246, <https://doi.org/10.1016/j.chemosphere.2021.132246>.
- [53] B. Pan, Y. Wu, B. Rhimi, J. Qin, Y. Huang, M. Yuan, C. Wang, Oxygen-doping of ZnIn<sub>2</sub>S<sub>4</sub> nanosheets towards boosted photocatalytic CO<sub>2</sub> reduction, *J. Energy Chem.* 57 (2021) 1–9, <https://doi.org/10.1016/j.jechem.2020.08.024>.
- [54] J. Yang, H. Miao, J. Jing, Y. Zhu, W. Choi, Photocatalytic activity enhancement of PDI supermolecular via  $\pi$ - $\pi$  action and energy level adjusting with graphene quantum dots, *Appl. Catal. B-Environ.* 281 (2021), 119547, <https://doi.org/10.1016/j.apcatb.2020.119547>.
- [55] Z. Zhu, H. Pan, M. Murugananthan, J. Gong, Y. Zhang, Visible light-driven photocatalytically active g-C<sub>3</sub>N<sub>4</sub> material for enhanced generation of H<sub>2</sub>O<sub>2</sub>, *Appl. Catal. B-Environ.* 232 (2018) 19–25, <https://doi.org/10.1016/j.apcatb.2018.03.035>.
- [56] J. Xu, B. Zhang, Y. Lu, L. Wang, W. Tao, X. Teng, W. Ning, Z. Zhang, Adsorption desulfurization performance of PdO/SiO<sub>2</sub>@graphene oxide hybrid aerogel: influence of graphene oxide, *J. Hazard. Mater.* 421 (2022), 126680, <https://doi.org/10.1016/j.jhazmat.2021.126680>.
- [57] L. Xu, J. Su, A. Ali, Q. Chang, J. Shi, Y. Yang, Denitrification performance of nitrate-dependent ferrous (Fe<sup>2+</sup>) oxidizing *Aquabacterium* sp. XL4: adsorption mechanisms of bio-precipitation of phenol and estradiol, *J. Hazard. Mater.* (2021), 127918, <https://doi.org/10.1016/j.jhazmat.2021.127918>.